Fast and accurate generation method of PSF-based system matrix for PET reconstruction*

Xiao-Li Sun(孙校丽)[1,2,3] Shuang-Quan Liu(刘双全)[1,2] Ming-Kai Yun(贠明凯)[1,2]
Dao-Wu Li(李道武)[1,2] Juan Gao(高娟)[1,2] Mo-Han Li(李默涵)[1,2,3] Pei Chai(柴培)[1,2]
Hao-Hui Tang(唐浩辉)[1,2] Zhi-Ming Zhang(章志明) [1,2] Long Wei(魏龙)[1,2;1)]

[1] Institute of High Energy Physics, Chinese Academy of Sciences, Beijing 100049, China
[2] Beijing Engineering Research Center of Radiographic Techniques and Equipment, Beijing 10049, China
[3] University of Chinese Academy of Sciences, Beijing 100049, China

Abstract: This work investigates the positional single photon incidence response (P-SPIR) to provide an accurate point spread function (PSF)-contained system matrix and its incorporation within the image reconstruction framework. Based on the Geant4 Application for Emission Tomography (GATE) simulation, P-SPIR theory takes both incidence angle and incidence position of the gamma photon into account during crystal subdivision, instead of only taking the former into account, as in single photon incidence response (SPIR). The response distribution obtained in this fashion was validated using Monte Carlo simulations. In addition, two-block penetration and normalization of the response probability are introduced to improve the accuracy of the PSF. With the incorporation of the PSF, the homogenization model is then analyzed to calculate the spread distribution of each line-of-response (LOR). A primate PET scanner, Eplus-260, developed by the Institute of High Energy Physics, Chinese Academy of Sciences (IHEP), was employed to evaluate the proposed method. The reconstructed images indicate that the P-SPIR method can effectively mitigate the depth-of-interaction (DOI) effect, especially at the peripheral area of field-of-view (FOV). Furthermore, the method can be applied to PET scanners with any other structures and list-mode data format with high flexibility and efficiency.

Keywords: PSF, P-SPIR, system matrix, GATE, PET reconstruction

PACS: 87.57.nf, 87.57.uk, 87.57.cf, **DOI:** 10.1088/1674-1137/41/4/048201

1 Introduction

Point spread function (PSF) has been proved effective for restoration of the tomographic image and widely used in positron emission tomography (PET) reconstruction [1]. Studies indicate that it improves the spatial resolution of PET systems [2–5] and mitigates the depth of interaction (DOI) effect [6–8] especially at the peripheral area of field-of-view (FOV). PSF describes the detector response distribution. Traditionally, PSF can be obtained through experimental measurements [9, 10], Monte Carlo-based simulations [11, 12], and analytical derivations [13–15]. However, the precise orientation of point sources in the experiment, the high costs of computing resources in the simulation, and the accuracy and rationality of the analytical methods are bottlenecks for traditional methods. Considering the properties of coincidences and lines of response (LOR) in PET, single photon incidence response theory (SPIR) was proposed by Fan et al in 2015 [16]. Nevertheless, this method still needs to be improved.

In this work, the positional single photon incidence response (P-SPIR), derived from SPIR, is proposed to obtain more accurate PSF for PET reconstruction. Additionally, the penetration effect occurring in two neighboring blocks is taken into consideration and a homogenization model is provided to generate the system matrix based on the response of single photons simulated on GATE [17]. With a PSF-based system matrix, further analysis is carried out on reconstruction images. For PET systems, emission data acquired from the PET scanner can be structured into distributed sinogram format and list-mode format. With improved contrast to noise performance, iterative reconstruction methods are widely used in clinical practice over analytical reconstruction methods. Based on OSEM (ordered subset expectation maximization) reconstruction with sinograms [18], full-width at half-maximum (FWHM) was analysed

Received 20 August 2016
* Supported by National Natural Science Foundation of China (81301348) and China Postdoctoral Science Foundation (2015M570154)
1) E-mail: weil@ihep.ac.cn

with reconstruction images of point sources, PET resolution was measured with a Derenzo phantom and image-quality assessment was carried out using NEMA NU 4-2008 standards [19] for a small-animal PET scanner in the Eplus-260 PET system. Results show that P-SPIR improves the image spatial resolution and image quality with lower computing costs and higher generation speed. Furthermore, this method can also be applied to reconstruction with list-mode data [20].

2 Method

Derived on the single photon incidence model, this work proposes a position-based method which is more thorough and meticulous than SPIR. Furthermore, compared with traditional methods, it is more convenient, effective and speedy in system matrix generation for PET reconstruction.

2.1 Positional SPIR model

SPIR theory takes a starting point that simulated response distributions can be applied in other PET systems when the crystal size is the same. This theory separates the simulation work from the concrete structure of the detector. However, in fact, the SPIR model, which takes only the incidence angle into account, cannot precisely describe the response distribution. Throughout the simulation, the P-SPIR model takes both incidence angle and incidence position into consideration. Furthermore, P-SPIR theory solves the problem of the gap influence when the penetration effect occurs in two neighboring blocks based on an analytical calculation. This effect has been proved to significantly and consistently reduce the computing cost under the circumstance of a good system matrix being generated and the image quality being improved.

2.1.1 Response model

The penetration effect is found to determine the response distribution, in addition to the incidence position, where the gamma photon is injected into the crystal array. In a previous paper, the point used to determine the response distribution after the incidence always lies along the angle of incidence. As in the SPIR model, the angle of incidence is simulated from 0 to 60° in 5° intervals, as shown in Fig. 1. However, there will be significant differences when considering the incidence position, as shown in Fig. 2. The P-SPIR response model divides each discrete crystal bar into x equal parts. In Fig. 2, the 7th crystal bar is divided into eight equal segments (x=8). Details are analysed with the same angle of incidence but different incidence positions in the same crystal bar, as shown in Fig. 3. On the GATE simulation platform, the incidence direction is controlled with a biased source. It is set that the number of source particles is M, and the count number of the ith crystal bar is M_i (i=0, 1, 2...15). So the response probability [21] of crystal i is

$$\rho_i = \frac{M_i}{M} \times 100\% \ . \tag{1}$$

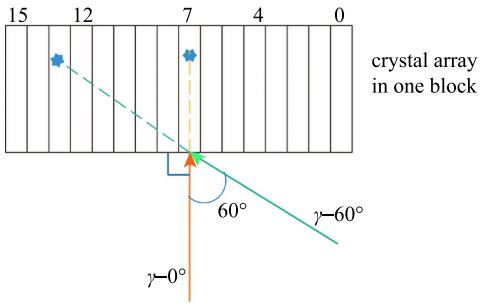

Fig. 1. (color online) Response model of SPIR. The midpoint of crystals is the incident position. Star markers indicate energy deposition.

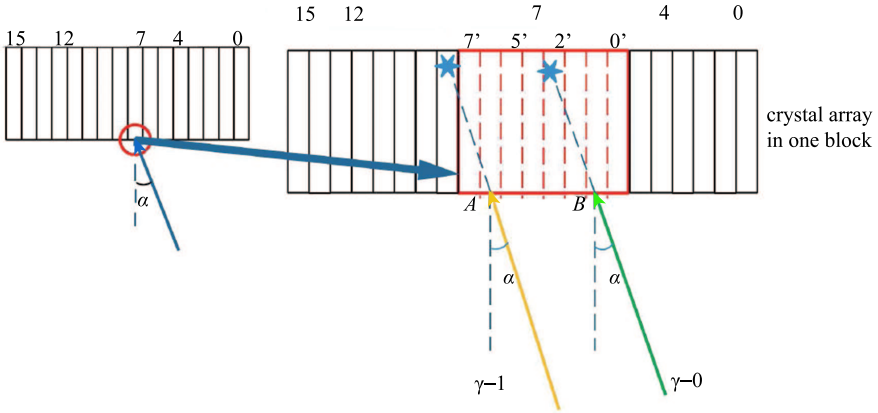

Fig. 2. (color online) Response model of P-SPIR. The red outlines represent the crystal in the red circle on the left-hand side of the diagram. The crystal of interest (the 7th) can be divided into n subdivisions with a certain incidence angle α. n is equal to 8 on the right, with α=0',1',2',3',4',5',6',7'.

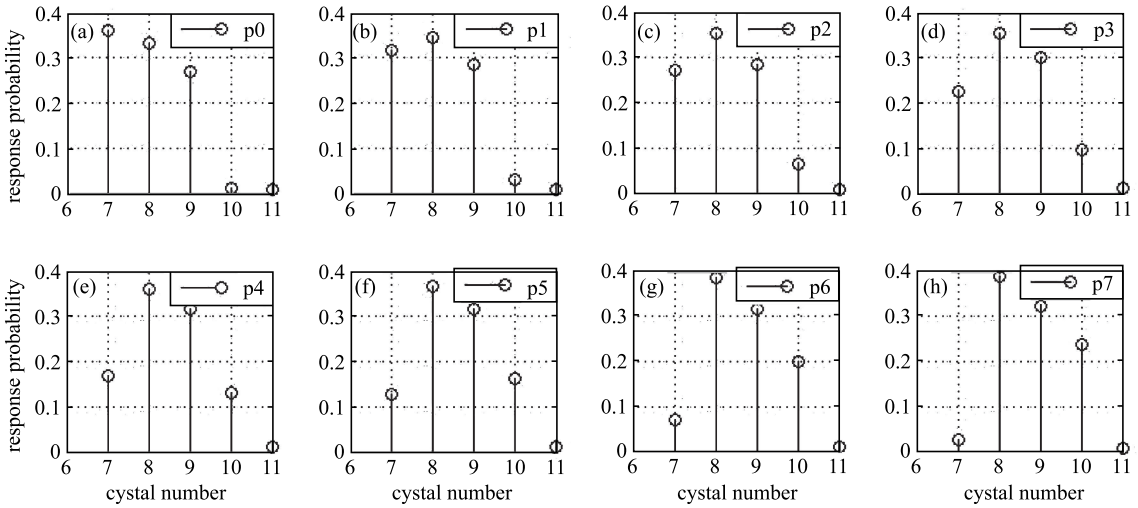

Fig. 3. (color online) Response distribution of different incidence positions with the same incidence angle at 30°. (a) to (h) show the results for different incident positions at 0',1',2',3',4',5',6',7', as described in Fig. 2.

When α in Fig. 2 is equal to 30°, the distributions in Fig. 3(a) to (h) show the response distribution of the 0th to 7th incidence position of the 7th crystal at 30°. Based on an overview of the data in Fig. 3, the peak position and peak value differ with the change of incidence position in a single crystal bar. Firstly, the peak position changes. For curve p0, the maximum is at the 7th crystal, whereas the others achieve their maximum at the 8th crystal. Secondly, p1, p2, and p7 share the same peak position but have significantly different distributions. The accuracy of the distribution is found to be of great importance in the calculation of the system matrix.

2.1.2 Process of gap influence

On the edge of the block, the penetration effect may occur between two neighboring blocks, as shown in Fig. 4. In the SPIR model, the particularity of the gap is almost ignored. After further study with GATE-based simulation, γ photons detected at the next block can occupy a large proportion at relatively large incidence angles, as shown in Fig. 5. It is assumed that the order number of one block is from 0 to 15, and 16 to 31 refers to the next block. Thus, the 15th crystal and the 16th crystal are close to each other but divided by the

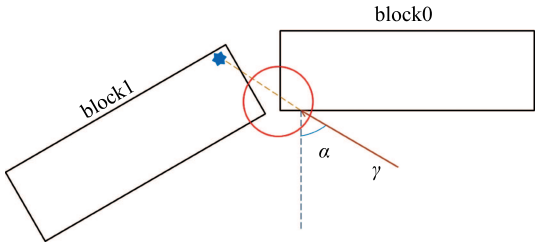

Fig. 4. (color online) The gap between two blocks is shown in the red circle. When a photon is incident on block0 at a certain angle and position, energy deposition can happen in the neighbouring block1. The photon can then be detected as a signal produced in block1.

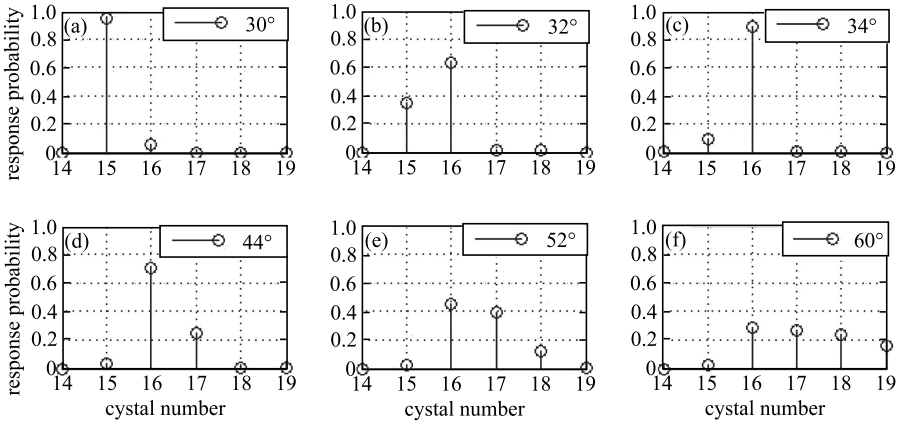

Fig. 5. Distribution of two neighboring blocks with different incidence angles (30°, 32°, 34°, 44°, 52° and 60°) on the 7th position of the 15th crystal.

gap. The curves indicates different incidence angles at the same incidence position of the 7th position of the 15th crystal. The distributions illustrate that the neighboring block with crystals from 16 to 31 dominates over the injected block with crystals from 0 to 15 with the penetration effect. As a result, the penetration effect between neighboring blocks should be carefully considered.

When the gap between two neighboring blocks is taken into account, P-SPIR theory will become invalid for separating the concrete detector structure, which reduces the superiority and the novelty of the simulation. Thus, the gap relationship indicated by a circle in Fig. 4 is solved with an analytical calculation method provided in Fig. 6.

The formula for the equivalent incidence angle into the next block β is

$$\beta=\alpha-\frac{2\pi}{R}\ , \tag{2}$$

where R is the block number in one ring, and α is the original incidence angle.

The formula for the equivalent incidence position in the next block AP^1 is

$$AP^1=\sigma+\frac{\sin(\pi/2-\alpha)}{\sin(\pi/2+\beta)}(\sigma+\nu), \tag{3}$$

$$p=\frac{AP^1}{\lambda}\ , \tag{4}$$

where λ is the transaxial width of the crystal, σ is the length of the gap size (i.e., AB and BC in Fig. 6), and ν is the distance from the incidence position to the edge (i.e., CP^0). p is the suppositional incidence position in block1.

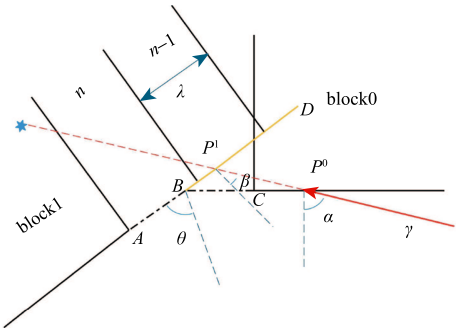

Fig. 6. (color online) Approximate calculation model for the gap. AB and BC indicate the gap between two neighboring blocks. BD is the extension line of AB. The nth and $n-1$th crystals between two blocks are virtual crystal bars (consistent with actual crystal bars) on the extended line of the crystal array of block1 to calculate the incidence position p on block1.

When the incidence angle β and the incidence position p are obtained, the distribution response of block1 can be calculated with the response model described in 2.1.1.

2.1.3 Normalization

In the simulation, the source activity and simulation time (corresponding to the acquisition time in the experiment) set in the GATE files are fixed, despite having different incidence directions and positions. However, as the counting rate is affected by specific physical factors, the counting rate becomes significantly different. Thus, the response distributions should be corrected with their respective detection efficiency. For example, if the source activity is A, the simulation time is t, and the number of effective singles detected (in total) is M, the formula for the counting rate η is

$$\eta=\frac{M}{At}\times 100\%\ . \tag{5}$$

The response probability of one crystal bar for a given incidence angle and position in the overall PET system is given by

$$\rho_{\rm norm}=\eta\rho_{\rm orig}\ , \tag{6}$$

where $\rho_{\rm orig}$ is the response probability calculated in Eq. (1).

2.2 Probability calculation

In the PET system, a line-of-response (LOR) consists of two gamma photons A and B with the same energy but opposite directions generated at the same time by an annihilation reaction. The LOR's proportion in the overall system is

$$\rho_{\rm LOR}=\rho_{\rm A\_norm}\rho_{\rm B\_norm}\ . \tag{7}$$

where $\rho_{\rm A\_norm}$ and $\rho_{\rm B\_norm}$ are the proportions of the two gamma photons.

2.3 System matrix generation

With response distributions derived from the P-SPIR model, a homogenization model is provided to generate the system matrix voxel-by-voxel.

The system matrix is developed with LOR distributions of voxels according to the dimensions of the reconstruction image. The homogenization theory hypothesizes that an ideal point source emits isotropic gamma photons with equal probability throughout the space. The ideal point source is placed (with its geometric volume ignored) in the center of the voxels, as shown in Fig. 7. The proportions of emitted $\rm LOR_1$, $\rm LOR_2$, $\rm LOR_3$, and $\rm LOR_4$ are the same. The angle between $\rm LOR_i$ and the horizontal axis is

$$\theta_i=\frac{\pi}{k}i,(i=0,1,2,...,k-1)\ . \tag{8}$$

where k is the number of the LORs in the model. When k is sufficiently large, the LORs can be considered homogeneous. With the increase of k, computing cost increases. However, the result approaches a steady state at a certain value.

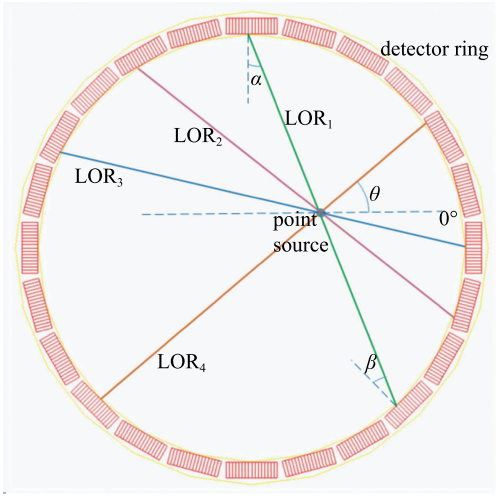

Fig. 7. (color online) Homogenization model. "Point source" represents the emission location. The dotted line is the reference axis and is set as 0 degrees. All LORs are considered in the equal probability emission. α and β are the incidence angles of the two particular single photons forming the LOR.

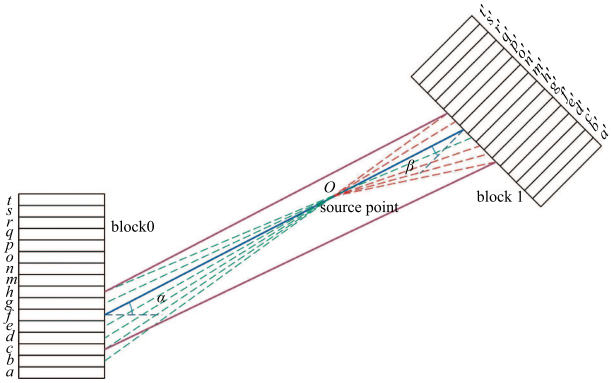

Fig. 8. (color online) The spread of LORs. The solid blue line is a LOR physically emitted from point O. The red dotted lines represent extensions detected in block0, similarly for the green dotted lines in block1.

Specifically, one homogeneous emission LOR above will be detected as several LORs account for the penetration effect, as shown in Fig. 8. For the LOR emitted in the homogeneous model, the incidence crystal number is f in block0 and n' in block1. The PSF describes the distribution incorporated with LORs formed by crystals b to f in block0 and o' to f'. Therefore, the detected LORs can be the combination of b to f and o' to f'. Ultimately, the proportion of one LOR combined with the ith and jth crystal is

$$\rho_{\mathrm{LOR}} = \sum_{0}^{k-1} \rho_i \rho_j \ . \tag{9}$$

2.4 Comparison of P-SPIR and simulation method

Voxel-by-voxel simulation is a traditional method to generate a system matrix [22, 23]. It requires a very long computing time, about a few months with a single-core computer, to meet data needs, and depends on the PET structure. The computing cost can be large, even though symmetry is taken into consideration, as shown by previous studies. However, the computing time of P-SPIR can be much less than 1 s with a single-core computer. Furthermore, it is much more meaningful than time saved that the system matrix can be achieved with the detector settings based on P-SPIR when the crystal model is the same. Consequently, P-SPIR has significant advantages when performing system matrix generation.

3 Results

Measurements have been carried out with the Eplus-260 Primate PET scanner designed by the Institute of High Energy Physics, Chinese Academy of Sciences (IHEP). This system is suitable for functional imaging of the heads of primates or the entire bodies of rodents. The scanner has good spatial resolution and detection efficiency. It contains high-performance LYSO crystals and position-sensitive photomultiplier tubes. The scanner has two rings, each containing 24 detector modules. Each module contains an array of 16 × 16 crystals with dimensions of 2 mm × 2 mm × 10 mm. The system has 768 crystals in total, and 32 rings with a pitch of 2 mm. Its FOV is a cylinder of dimensions 190 mm transaxially and 64 mm axially. For the Eplus-260 Primate PET scanner, the image space and the LOR histogram configuration are listed in Table 1.

Table 1. Image volume and LOR histogram parameters.

settings	value
number of angles	192
bins per angle	199
image voxels	380×380×63
voxel size/mm^3	0.5×0.5×1.0

For the Eplus-260 Primate PET, the voxels in a quarter of the FOV are used as the basic matrix. The distribution of LORs is calculated as in Eq. (9). The distribution of voxels in other regions can be obtained by symmetry. So the system matrix that needs to be stored

has a dimension of 190×190×192×10, and the storage requirement is 554.496 Mb.

Both simulation data and experimental data are reconstructed based on OSEM. FWHMs of simulated points, the reconstruction image of Derenzo phantom and image-quality phantom are analyzed.

3.1 FWHM of point sources

Point sources at the radial positions of 5, 10, 15, 25, 50 and 75 mm, as per the National Electrical Manufactures Association (NEMA) guidelines, were simulated on the GATE platform. The source activity was as low as possible to ensure true coincidences at 2×10^6 Bq, and the total count number was about 3×10^6 counts. To improve simulation efficiency, back-to-back source type was used. The FWHW of the reconstruction image was analyzed, as shown in Fig. 9. On one hand, the reconstruction image of the point source close to the edge is significantly expanded without PSF. On the other hand, the FWHM of the point with PSF is much improved, particularly at the positions of 50 mm and 75 mm off-center, which means that the DOI effect is significantly mitigated in the edge regions.

3.2 Derenzo phantom

The Derenzo phantom [24, 25] was measured on the Eplus-260 Primate PET system. ^{18}F was used with a total activity of 0.8 mCi. The acquisition time was 20 minutes. The image reconstruction using OSEM, OSEM-PSF with voxel-by-voxel Monte Carlo-based simulation, and OSEM-PSF with P-SPIR, is shown in Fig. 10. This

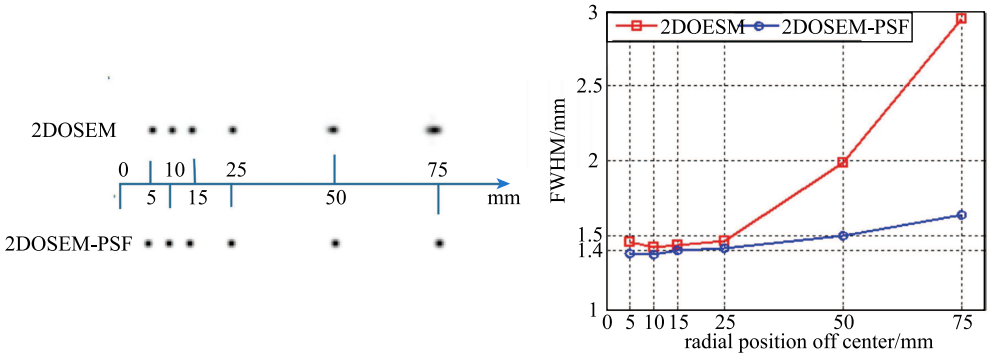

Fig. 9. (color online) Reconstruction images of point sources. On the left are the reconstructed images of points radially off-center by 5, 10, 15, 25, 50, and 75 mm with 2DOSEM and 2DOSEM-PSF. On the right are the FWHMs of the points at different positions.

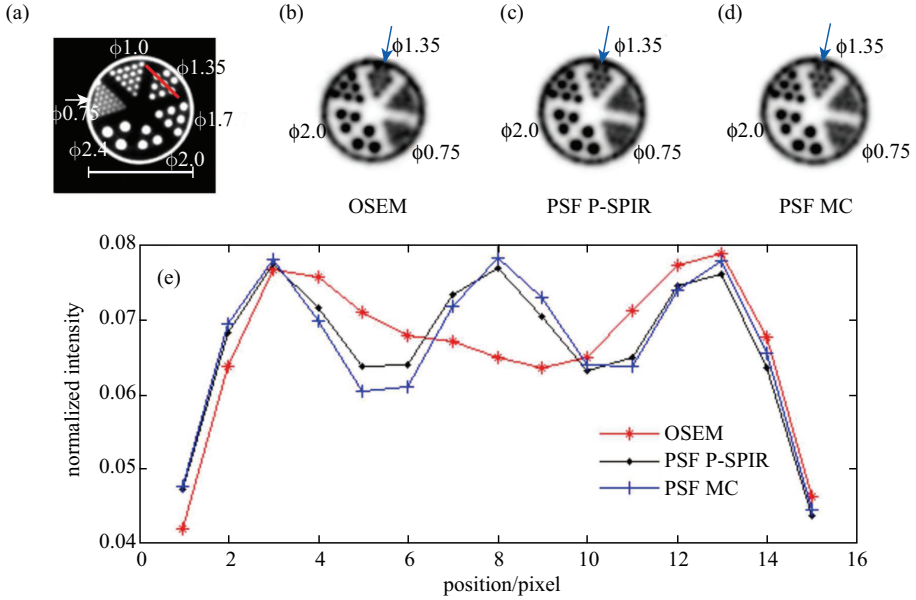

Fig. 10. (color online) Reconstruction images of the Derenzo phantom. (a) shows the phantom model used in the experiments, (b) is the reconstructed image with traditional OSEM, (c) is with PSF derived from P-SPIR and (d) is with PSF derived from voxel-by-voxel simulation based on Monte Carlo. (e) are profiles of (b), (c) and (d) along the direction of the red line in (a).

figure shows the 28th slice reconstructed with 4 iterations and 24 subsets; it clearly indicates that the reconstruction method with PSF is able to distinguish the point sources in the 1.35 mm-field, as compared to the non-PSF method. Furthermore, the profiles reveal that the curve peaks with PSF are better defined as three points along the red line than the OSEM without PSF. The result derived from the method with P-SPIR is consistent with the Monte Carlo simulation method.

3.3 Image quality

The phantom used in the experiment to analyse image quality is according to NEMA NU 4-2008 guidelines. ^{18}F was used, with a total activity of 100 μCi. The phantom was placed on the animal bed to make the axis of its main cylindrical compartment aligned with the axis of the tomograph FOV. The data acquisition time was 10 min.

%STD (percentage standard deviation), RC (recovery coefficient)and SOR (spill-over ratio) are examined to analyze the image quality. Figure 11 shows the same transverse slice of a NEMA NU 4-2008 image-quality phantom reconstruction image with PSF and without PSF. The iterative condition in the reconstruction was the same with 4 iterations and 24 subsets. The percentage SD obtained in the uniform region with OSEM and PSF-OSEM based on P-SPIR, with all the corrections applied, was 5.34% and 3.85% respectively. The SORs measured in the air- and water- filled chambers of the NEMA phantom after all the corrections applied were 3.79% and 5.66% with OSEM, respectively, while with PSF-OSEM the SORs were 3.39% and 4.51%. RCs measured for the five different rod diameters with 1, 2, 3, 4, 5mm are shown in Fig. 11.

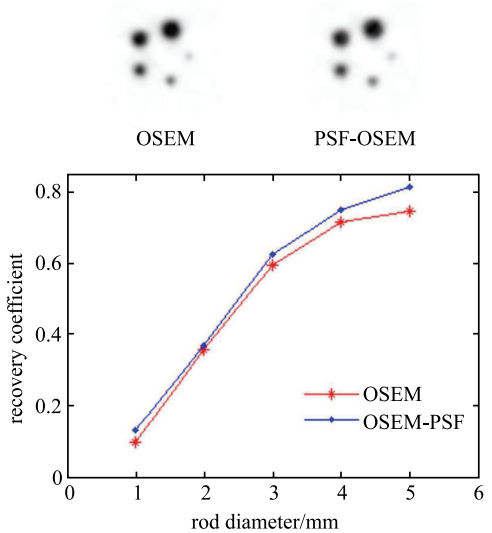

Fig. 11. (color online) RCs of different rods reconstructed based on OSEM2D with PSF and without PSF.

3.4 Computational performance analysis

Reconstruction with PSF can have a long running time. The parallel computing power of the GPU [26], with multiple processor cores which can handle threads in parallel, is utilized to reduce the reconstruction time. Because of the relatively small size of the system matrix, the matrix can be loaded directly into memory of a GPU. On-the-fly forward and backward projectors are implemented with specific GPU kernels in a 'voxel-driven' manner to suit the format of system matrix voxel-by-voxel. With the parallel computing of the GPU, voxels are in parallel processing as parallel threads rather than serial processing, which greatly reduces run time. Additionally, to solve the problem of memory access conflict in the forward projector, atomic operations are applied. A comparison of the methods with or without GPU (NVIDIA GeForce GTX 660) is presented in Table 2. The computing time with GPU is less than 10 percent of the time taken with CPU (Intel core i5-2400), which makes it suitable for clinical applications.

Table 2. Comparison of the PSF methods with CPU and GPU for (380 × 380 × 63) with one iteration under the same conditions.

reconstruction method	computing time/s
CPU	479
GPU	43

Additionally, in a given voxel, there will be 199 bins for each angle. Mostly, the proportion is close to zero. Taking all of the bins into consideration for PET reconstruction might result in a large computing cost, which will make it extremely difficult to meet the requirements of clinical applications. Accordingly, the number of extended bins of each angle should be truncated in N with descending order. It is a tradeoff between the accuracy of the system matrix and the computing cost. The reconstruction images with different values of N are shown in Fig. 12. The reconstruction time cost with GPU is provided in Table 3.

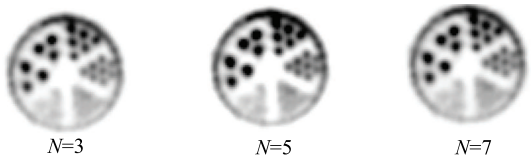

Fig. 12. Reconstruction comparison with different values of N for the same slice.

Figure 12 indicates that the results are almost the same for N = 3, 5, and 7. However, the storage requirement and reconstruction time increase with the growing of N. In applications on the Eplus-260 Primate PET, N = 5 is chosen as a conservative number.

Table 3. Reconstruction time of image comparison for different values of N.

N	reconstruction time with GPU/s
3	38
5	43
7	113

4 Discussion and conclusions

The system matrix is necessary and important for iterative methods in PET reconstruction. However, the generation of the system matrix can be a difficult task for experimental methods and Monte Carlo simulation methods. In this paper, a positional SPIR method, named P-SPIR, is presented. It is a precise model to improve the accuracy of the system matrix and reduce the computing costs (i.e., both the computing time and the storage capacity). Furthermore, analytical calculation of the gap process and system matrix generation based on the homogenization model reinforce its reusability, portability, and interoperability for PET systems, especially when the crystal size is the same. A database can even be derived from the S-SPIR model with a wide range of crystal sample sizes and types of crystal material. As a result, the system matrix for a particular PET system can be rapidly and efficiently generated on-line with only system configuration. The improvement of spatial resolution has been proven with both simulation data and experimental data on the Eplus-260 Primate PET system. However, several problems in applications should be discussed. Firstly, although the method has been applied to the Eplus-260 Primate PET system, more support for other PET systems may be needed to validate its applicability and convenience. Secondly, despite the above-mentioned advantages, other performance should be analysed q antitatively. Thirdly, the influence of the selection of subdivision number for the crystal should be demonstrated in further detail. Finally, correction [27] should be taken into consideration to acquire images that are more conducive to diagnosis and treatment.

Reconstruction results provided in this paper are based on sinograms. However, theoretically speaking, P-SPIR and methods to generate accurate system matrices can also be applied to emission data format in list-mode. Accordingly, list-mode reconstruction with P-SPIR is the direction of further research.

References

1 B. Karuta and R. Lecomte, IEEE Trans. Med. Imaging, **11**(3): 379–385 (1992)
2 V. Andrea, S. Nils, E. Lars et al, Eur. J. Nucl. Med. Mol. Imaging, **36**(10): 1639–1650 (2009)
3 J. Thies, Z. Vilia, S. Jessica et al, Eur. J. Nucl. Med. Mol. Imaging, **3**(1): 1–17 (2016)
4 T. Thonnapong, I. Yoko, S. Takahiro et al, Radiological Physics and Technology, **9**(1): 127–137 (2016)
5 K. Kazuya, K. Kenichi, T. Makiko et al, British journal of radiology, **89**(1063): 20150938 (2016)
6 V. Astakhov, P. Gumplinger, C. Moisan et al, IEEE Transactions on Nuclear Science, **50**(5): 1373–1378 (2003)
7 S. Salvador, D. Huss, D. Brasse et al, IEEE Transactions on Nuclear Science, **56**(1): 17–23 (2009)
8 M. Ito, J. S. Lee, S. I. Kwon et al, IEEE Transactions on Nuclear Science, **57**(3): 976–981 (2010)
9 V. Y. Panin, F. Kehren, H. Rothfuss et al, IEEE Transactions on Nuclear Science, **53**(1): 152–159 (2006)
10 S. Tong, A. M. Alessio and P. E. Kinahan. Phys. Med. Biol, **55**(5): 1453–1473 (2010)
11 K. Lee, P. E. Kinahan, J. A. Fessler et al, Phys. Med. Biol, **49**(19): 4563–4578 (2004)
12 K. Saha, K. J. Straus, Y. Chen et al, J. Appl. Phys, **116**(8) (2014)
13 J. Qi, R. M. Leahy, S. R. Cherry et al, Phys. Med. Biol, **43**(4): 1001–1013 (1998)
14 R. T. Yao, R. M. Ramachandra, N. Mahajan et al, Phys. Med. Biol, **57**(21): 6827–6848 (2012)
15 A. Lougovski, F. Hofheinz, J. Maus et al, Phys. Med. Biol, **59**(3): 561–577 (2014)
16 X. Fan, H. P. Wang, M. K. Yun et al, Chin. Phys. B, **24**(1): 500–542 (2015)
17 K. Assié, V. Breton, I. Buvat et al, Nucl. Instrum. Methods Phys. Res., Sect. A, **527**(1): 180–189 (2004)
18 M. Cañadas, P. Arce, M. P. Rato, Phys. Med. Biol, **56**(1): 273–288 (2011)
19 National Electrical Manufacturers Association (NEMA), NEMA Standards Publication NU 4-2008: Performance Measurement for Small Animal Positron Emission Tomographs (Washington, DC: NEMA, 2008)
20 I. J. Ahn, J. H. Kim, Y. J. Chang et al, IEEE Transactions on Nuclear Science, **62**(3): 859–868 (2015)
21 M. Rafecas, B. Mosler, M. Dietz et al, IEEE Transactions on Nuclear Science, **51**(5): 2597–2605 (2004)
22 F. R. Rannou, A. F. Chatziioannou, IEEE Symposium Conference Record Nuclear Science 2004, **6**: 3433–3436 (2004)
23 J. D. Leroux, C. Thibaudeau, R. Lecomte and R. Fontaine, 2007 IEEE Nuclear Science Symposium Conference Record, **5**: 3644-3648 (2007)
24 F. Boisson, C. J. Wimberley, W. Lehnert et al, Phys. Med. Biol, **58**(19): 6749–6763 (2013)
25 L. Y. Wang, J. Zhu, X. Liang et al, Phys. Med. Biol, **60**(1): 137–150 (2015)
26 J. Zhou and J. Y. Qi, Phys. Med. Biol, **56**(20): 6739–6757 (2011)
27 M. Aykac, V. Y. Panin, I. Hong and M. E. Casey. 2014 IEEE Nuclear Science Symposium and Medical Imaging Conference, 1–5 (2014)